Creep Performance Modeling of Modified 9Cr-1Mo Steels with Oxidation

X.J. WU, X.Z. ZHANG, R. LIU, and M.X. YAO

In this study, the deformation-mechanism-based true-stress (DMTS) creep model is modified to include oxidation influence on the long-term creep performance of modified 9Cr-1Mo steels. An area-deduction method is introduced to evaluate oxide scale formation on the creep coupons, which is incorporated into the DMTS model formulated based on intragranular dislocation glide (IDG), intragranular dislocation climb (IDC), and grain boundary sliding (GBS) mechanisms, in modifying the true stress. Thus, the modified DMTS model can not only describe the creep curve, but also predict the long-term creep life and failure mode, which is shown to be in good agreement with the creep data generated in the authors' laboratory as well as by the National Institute for Materials Science (NIMS) of Japan for long-term ($> 10^4$ hours) creep life prediction on Grade 91 steels. In particular, the predictability of the model is demonstrated in comparison with the Larson–Miller parameter method. In addition, the modified DMTS model provides quantitative information of mechanism partitioning, insinuating the failure mode *via* intragranular/intergranular deformation. Therefore, it has advantages over the empirical models in providing physical insights of creep failure, which can be useful to material design for performance optimization.

I. INTRODUCTION

CREEP phenomena have been studied for more than 100 years, ever since Andrade first observed time-dependent flow of metals under constant load in 1910.[1] Most of the steady-state creep mechanisms were classified into deformation-mechanism maps by Frost and Ashby.[2] Langdon,[3] Lüthy *et al.*,[4] and Wu and Koul[5] also recognized grain boundary sliding as an important deformation mechanism inducing transient creep behavior. However, with regard to creep lifetime prediction, the existing models are mostly data-extrapolation methods such as the Larson–Miller parameter method,[6] the Monkman–Grant relation,[7] and the Wilshire equation,[8] which were established *via* short-term creep tests. Prediction of long-term creep life remains to be a challenging task faced by the power-generation industry.[9]

Among the factors influencing materials' creep performance, oxidation is an important degradation mechanism. Inevitably, metal oxidation will occur under high-temperature creep test conditions in air, which will definitely have an impact on materials' creep behavior. However, studies to quantify the oxidation effects on creep rate and creep life have been rarely reported, since vacuum creep tests are almost cost-prohibitive for long-term experiments such that oxidation-free creep data are unavailable for most materials. Most creep data are generated in air with coupon-borne influence of oxidation, and thus empirical creep life prediction methods based on such short-term creep data are questionable, because the extrapolation for prediction of long-term creep performance using these methods does not consider the influence of oxidation as a time-dependent factor. This problem has long been encountered in engineering. For example, long-term creep rupture data generated by the National Institute for Materials Science (NIMS) show that there is a life breakdown phenomenon for Grade 91 steels, especially at high temperatures.[10–12] The in-service experience reviewed by the Electric Power Research Institute (EPRI) of USA demonstrates that "cracking in creep-strength enhanced ferritic (CSEF) steel components has occurred relatively early in life. In many cases, the occurrence of damage has been linked to less than optimal control of steel making, processing, and component fabrication."[13] Apparently, the current creep

X.J. WU is with the Structures and Materials Performance Laboratory, Aerospace Research Center, National Research Council Canada, Ottawa, ON, K1A 0R6 Canada. Contact e-mail: Xijia.Wu@nrc-cnrc.gc.ca X.Z. ZHANG and R. LIU are with the Department of Mechanical and Aerospace Engineering, Carleton University, Ottawa, ON, K1S 5B6 Canada. M.X. YAO is with the Kennametal Stellite Inc., Belleville, ON, K8N 1G2 Canada.

life prediction methodology has missed some life-limiting factors for long-term creep—oxidation is one of them.

The continuum damage mechanics approach considered the oxidation effect in a single power-law formulation of creep rate.[14,15] As demonstrated in the previous studies on modified 9Cr1Mo steels and Waspalloy,[16,17] the creep behavior over a wide range of stress (~ 0.1-0.9 UTS) can be depicted by the deformation-mechanism-based true-stress (DMTS) creep model constituted based on intragranular dislocation glide (IDG), intragranular dislocation climb (IDC), and grain boundary sliding (GBS) mechanisms, each exhibiting a distinct power-law behavior. Naturally, oxidation will affect the relative contributions of all the involved deformation mechanisms during long-term exposure to high temperature, as it reduces the cross-section area of the parent material.

In this study, first, an area-deduction method is introduced to evaluate the area loss due to oxidation, which is then incorporated into the DMTS creep model to correct for the true stress in material coupons during creep. Then, the oxidation-modified DMTS model is formulated to describe the creep curve and predict the failure mode and lifetime based on the mechanism partitioning involving IDG, IDC, GBS, as well as oxidation. Finally, the oxidation-modified DMTS model is achieved which can predict the long-term creep life of modified Grade 91 steels, showing good agreement with the NIMS data,[18] consistently across the Grade 91 steel products such as tubes, plate, and forging.

II. EXPERIMENTAL PROCEDURE AND MODELING

A. Materials and Experiments

Creep tests were conducted on an ASME SA182-01-specified F91 material. The composition, heat treatment, mechanical properties, coupon geometry with a gauge length of 0.791 inch and a diameter of 0.158 inch, and creep test details are reported in the previous research.[16] The tests were performed at 733 K, 823 K, 873 K, and 923 K (500 °C, 550 °C, 600 °C and 650 °C) under various stress levels from 80 to 320 MPa. After the creep tests, ruptured specimens were cut, both longitudinally and horizontally, at locations close to the ruptured surface but away from the necking zone. The sectioned specimens were polished following standard metallographic procedures, and then subjected to microstructural analysis using an Olympus GX71 optical microscope and Philips XL3053 scanning electron microscope (SEM) in the secondary electron (SE) imaging and backscattered electron (BSE) modes. The results of the creep tests and metallurgical examination are used to validate the model, while the creep rupture data from NIMS are used for comparison with the model prediction. The designations of the NIMS materials and their thermomechanical processing histories are given in Table I, along with F91 steel.

B. The DMTS Model with Oxidation Effect

Recall that the true-stress creep formulation for incompressible flow is based on the following true stress–strain definition[16,17]:

$$\sigma = \sigma_0 \exp(\varepsilon) \qquad [1a]$$

$$\varepsilon = \ln(1 + e), \qquad [1b]$$

where $\sigma_0 = P/A_0$ is the engineering stress, σ is the true stress, P is the applied load, A_0 is the original cross-section area of the specimen; e and ε are engineering and true strain, respectively.

When oxidation occurs, a layer of oxide grows on the specimen surface, following the parabolic law[19]:

$$\delta = \sqrt{2K_{ox}t}, \qquad [2]$$

where δ is the scale thickness; K_{ox} is the oxidation rate coefficient; and t is exposure time.

Because iron oxides are brittle and loose, oxidation can cause area reduction by an amount of $2\pi r\delta$. Then, according to Eq. [1a], the true stress at any time is given by

$$\sigma = \frac{P}{A_0 - 2\pi r\delta}\exp(\varepsilon) = \frac{P}{A_0(1 - \omega_{ox})}\exp(\varepsilon)$$
$$= \frac{\sigma_0}{1 - \omega_{ox}}\exp(\varepsilon), \qquad [3a]$$

where r is the radius of the specimen, and the areal loss by oxidation is defined by

$$\omega_{ox} = \frac{2\pi r\delta}{\pi r^2} = \frac{2\delta}{r}. \qquad [3b]$$

Considering the above modification of the true stress, the rate equation for GBS, IDG, and IDC can be written, respectively, as[16,17,20]:

$$\dot{\varepsilon}_s = A\sigma^p = A\left(\frac{\sigma_0}{1 - \omega_{ox}}\right)^p \exp(p\varepsilon) \approx \frac{1 + p\varepsilon}{(1 - \omega_{ox})^p}A\sigma_0^p$$
$$= \frac{1 + p\varepsilon}{(1 - \omega_{ox})^p}\dot{\varepsilon}_{s0} \qquad [4]$$

$$\dot{\varepsilon}_s = B\sigma^n = B\left(\frac{\sigma_0}{1 - \omega_{ox}}\right)^n \exp(n\varepsilon) \approx \frac{1 + n\varepsilon}{(1 - \omega_{ox})^n}B\sigma_0^n$$
$$= \frac{1 + n\varepsilon}{(1 - \omega_{ox})^n}\dot{\varepsilon}_{g0} \qquad [5]$$

$$\dot{\varepsilon}_c = (1 + M\varepsilon)C\sigma^m = (1 + M\varepsilon)C\left(\frac{\sigma_0}{1 - \omega_{ox}}\right)^m \exp(m\varepsilon)$$
$$\approx \frac{1 + M\varepsilon + m\varepsilon}{(1 - \omega_{ox})^m}C\sigma_0^m = \frac{1 + M\varepsilon + m\varepsilon}{(1 - \omega_{ox})^m}\dot{\varepsilon}_{c0}, \qquad [6]$$

where $\dot{\varepsilon}_{s0}, \dot{\varepsilon}_{g0}, \dot{\varepsilon}_{c0}$ are the initial strain rates at σ_0, and M is the dislocation multiplication factor.

Then, the total strain rate $\dot{\varepsilon}_v$ by physical deformation decomposition can be re-written into

Table I. Heat Treatment Histories of NIMS Materials[18]

Type	NIMS Code	Processing and Thermal History	Standard
Tube	MGD	hot extruded and cold drawn 1050 °C/10 min AC 780 °C/40 min AC	ASME SA-213/SA-213M Grade T91
	MgB	hot rolled 1050 °C/10 min AC 770 °C/60 min AC 740 °C/60 min FC	ASME SA-387/SA-387M Grade 91
	MgD	hot rolled 1050 °C/30 min AC 780 °C/30 min AC	
Pipe	MGQ	hot rolled 1060 °C/60 min AC 780 °C/60 min AC	ASME SA-335/SA-335M Grade P91
F91		forged 1080 °C/4 h AC 800 °C/5 h AC	ASME SA182-01Grade F91

AC: air cooling, FC: furnace cooling.

$$\dot{\varepsilon}_v = \dot{\varepsilon}_s + \dot{\varepsilon}_g + \dot{\varepsilon}_c$$
$$= \frac{1 + p\varepsilon}{(1 - \omega_{ox})^p}\dot{\varepsilon}_{s0} + \frac{1 + n\varepsilon}{(1 - \omega_{ox})^n}\dot{\varepsilon}_{g0} + \frac{1 + M\varepsilon + m\varepsilon}{(1 - \omega_{ox})^m}\dot{\varepsilon}_{c0}$$

[7a]

which can be re-arranged as

$$\dot{\varepsilon} = k(t) + h(t)\varepsilon$$

[7b]

where as δ and ω_{ox} depend on t by Eqs. [2] and [3b], so are

$$k(t) = \frac{1}{(1 - \omega_{ox})^p}\dot{\varepsilon}_{s0} + \frac{1}{(1 - \omega_{ox})^n}\dot{\varepsilon}_{g0} + \frac{1}{(1 - \omega_{ox})^m}\dot{\varepsilon}_{c0}$$

[7c]

$$h(t) = \left[\frac{p}{(1 - \omega_{ox})^p}\dot{\varepsilon}_{s0} + \frac{n}{(1 - \omega_{ox})^n}\dot{\varepsilon}_{g0} + \frac{m + M}{(1 - \omega_{ox})^m}\dot{\varepsilon}_{c0}\right].$$

[7d]

The first-order linear ordinary differential equation, Eqs. [7a] through [7d], has a general solution in the form:

$$\varepsilon = \exp\left[\int h(t)dt\right]\int_0^t k(\tau)\exp\left[-\int h(\tau)d\tau\right]d\tau.$$

[8]

When oxidation is absent (or negligible), *i.e.*, $\omega_{ox} = 0$, the integration of Eq. [8] leads to

$$\varepsilon = \frac{1}{M'}[\exp(M'kt) - 1],$$

[9]

where $M' = h/k$, as obtained in the previous work.[16,17]

For an oxidation-intervened process, the exact integration solution of Eq. [8] is difficult to obtained, given

the functional forms of $h(t)$ and $k(t)$ in Eqs. [7c] and [7d], but we can define a working boundary for Eq. [8], following the guidelines of ASME Code B31G, within which a simplified solution is sought. The ASME code generally does not allow the corrosion depth to exceed 10 pct of the pipe thickness for safe operation. Under the most severe oxidation condition, *i.e.*, at 923 K (650 °C), in the present study, IDC is the dominant mechanism with a power-law index of ~ 6, and the magnifying effect of 10 pct thickness reduction on creep rate is ~ 1.88, which is almost equal to the typical scatter bandwidth with the factor of 2 in the measured creep rate and creep life data. Therefore, given the experimental uncertainty, it is better to take engineering convenience and conservativeness over mathematical rigorousness within the bound of material property scatter. Therefore, Eq. [9] is chosen as the strain-integration form, but with k and M' taken as a function of time as defined by Eqs. [7a] through [7d]. The conservativeness is inferred from the Mean Value Theorem for Integrals, given that the integrands in Eq. [8] are monotonically increasing functions of time. Even though Eq. [9] is not mathematically rigorous, for the complex time-dependent process such as creep with so many factors that can cause the variation in the creep behavior, it is adequate to represent the physical interplay of the controlling mechanisms.

Oxidation during transient creep can be ignored, because of its short time, and hence, the total strain is described by adding the transient creep component,[5] as[16,17]

$$\varepsilon = \varepsilon_0 + \varepsilon_{tr}^P\left[1 - \exp\left(-\frac{t}{t_T}\right)\right] + \frac{1}{M'}[\exp(M'kt) - 1]$$

[10a]

$$\varepsilon_{tr}^P = \frac{\sigma}{\beta^2 H}$$

[10b]

$$t_{\mathrm{T}} = \frac{\sigma(\beta - 1)}{\beta^2 H \dot{\varepsilon}_{\mathrm{s}}}, \qquad [10c]$$

where β is the transient creep constant and H is grain boundary work-hardening coefficient.[5] Since primary creep stage is relatively short in the entire creep process, oxidation effect on primary creep can be negligible.

Equations [10a] through [10c] describes the creep strain–time response with the involved mechanism contributions as well as the oxidation effect, because M' and k include the oxidation-modified term for each mechanism, and it naturally reduces to the material-intrinsic behavior when oxidation effect is absent.

For long-term creep life prediction, the time-to-rupture (TTR) is much longer than the transient time, i.e., TTR $\gg t_{\mathrm{T}}$ so that the transient exponential term, $\exp\left(-\frac{t}{t_{\mathrm{T}}}\right)$, will vanish, and the failure strain will be much greater than the initial elastic strain ε_0, i.e., $\varepsilon_{\mathrm{cr}} \gg \varepsilon_0$, then Eqs. [10a] through [10c] can be re-arranged into

$$\mathrm{TTR} = \frac{1}{M'k}\ln\left[1 + M'\left(\varepsilon_{\mathrm{cr}} - \frac{\sigma}{H\beta^2}\right)\right], \qquad [11]$$

where $\varepsilon_{\mathrm{cr}}$ is the critical failure strain.

III. RESULTS AND DISCUSSION

A. Oxidation

The as-received microstructure of F91 (forging) contains a conventional martensitic lath structure with prior-austenite boundaries and $Cr_{23}C_6$ and MX precipitates, similar to the NIMS tube, plate and pipe materials, as reported by other researchers.[21–23] These microstructures are the baseline references for the following comparison studies.

Figure 1 shows the cross-section views of selected coupons after creep tests at temperatures from 733 K to 923 K (500 °C to 650 °C). It is seen that very thin oxide scales formed on the surfaces of 733 K to 823 K (500 °C to 550 °C)-exposed coupons, and that on the 873 K to 923 K (600 °C to 650 °C)-exposed coupons is much thicker. Most oxidation products on the 923 K (650 °C)-exposed coupon were spalled off, perhaps repeatedly, resulting in an irregular-shape surface layer, as opposed to the perfect circular cross section of the original coupons. The remaining cross-section area for each coupon after the creep test was measured using an image processing software, Adobe Photoshop and ImageJ.

Because the Fe-Cr-oxides (a mixture of Fe_3O_4, FeO, Fe_2O_3, and $(Fe, Cr)_3O_4$) are loose and can easily spall off the specimen surface during creep testing or specimen cutting,[24] direct measurement of the oxide scale would not give accurate results for oxidation scale evaluation. Here, an area-deduction method is proposed, as schematically shown in Figure 1(b), where the shadowed area represents the remaining cross section and the losses due to deformation and oxidation are also indicated. Using this method the oxide layer thickness

is evaluated as the original specimen cross-section area corrected by deformation minus the remaining unoxidized area, as expressed by

$$2\pi r\delta = \frac{A_0}{1 + \varepsilon_{\mathrm{cr}}} - A_{\mathrm{r}}, \qquad [12]$$

where $\varepsilon_{\mathrm{cr}}$ is defined as the critical creep strain attained at 90 pct of the time-to-rupture (TTR) (just before necking unstability occurred).

Assuming oxide scale forms uniformly on the specimen surface and the cross section remains nominally circular during the creep test, Eq. [12] provides an effective way to quantify the oxidation scale growth than direct measurement of the oxide scale remaining on the coupon, since the oxides could partially spall off during specimen testing and handling. The oxide scale thickness of ruptured F91 coupons under various creep test conditions is evaluated using Eq. [12], and the results are summarized in Table II, where the "nominal diameter at rupture" is calculated from the measurement of the unoxidized cross-section area, assuming a circular shape, and the other "losses" are deduced, according to Eq. [12] and the incompressible flow rule.

The oxidation behavior of P91 in the temperature range of 873-1073 K (600-800 °C) has been found to follow parabolic growth kinetics in weight gain as observed by Mathiazhagan and Khanna for up to 1000 hours.[25] Again, assuming the parabolic law of oxidation in terms of scale thickness growth, the oxidation rate coefficient (K_{ox}) for each test condition can be determined from the measurement, according to Eq. [12], as given in Table II. For the first-order approximation, the average K_{ox} at each temperature is expressed as an Arrhenius equation, and from the Arrhenius plot (Figure 2), the activation energy and proportional constant of K_{ox} are determined for F91 steel as

$$K_{\mathrm{ox}} = 2.04 \times 10^9 e^{-19698/T} \mu\mathrm{m}^2/\mathrm{h}. \qquad [13]$$

It should be noted that oxidation during creep is generally stress-dependent, because stress can affect the oxidation process in three ways: (i) diffusion of the oxidation species, (ii) local volume change by formation of oxide products, and (iii) repeated spallation that alters the path of diffusion of the oxidation species. However, there is no theoretical formula that can take all of these factors into account yet, and the evaluation in the present study is limited to establish an empirical relationship, as the area-deduction method is used the first time in creep study. Therefore, the oxidation rate is assumed to be constant per temperature condition, as the first-order approximation, for the present purpose. The area-deduction method provides a means to quantify oxidation growth kinetics during creep under stress, but extensive work needs to be done.

B. Creep Rupture

All the F91 coupons experienced necking followed immediately by rupture of the entire specimen. Figure 3
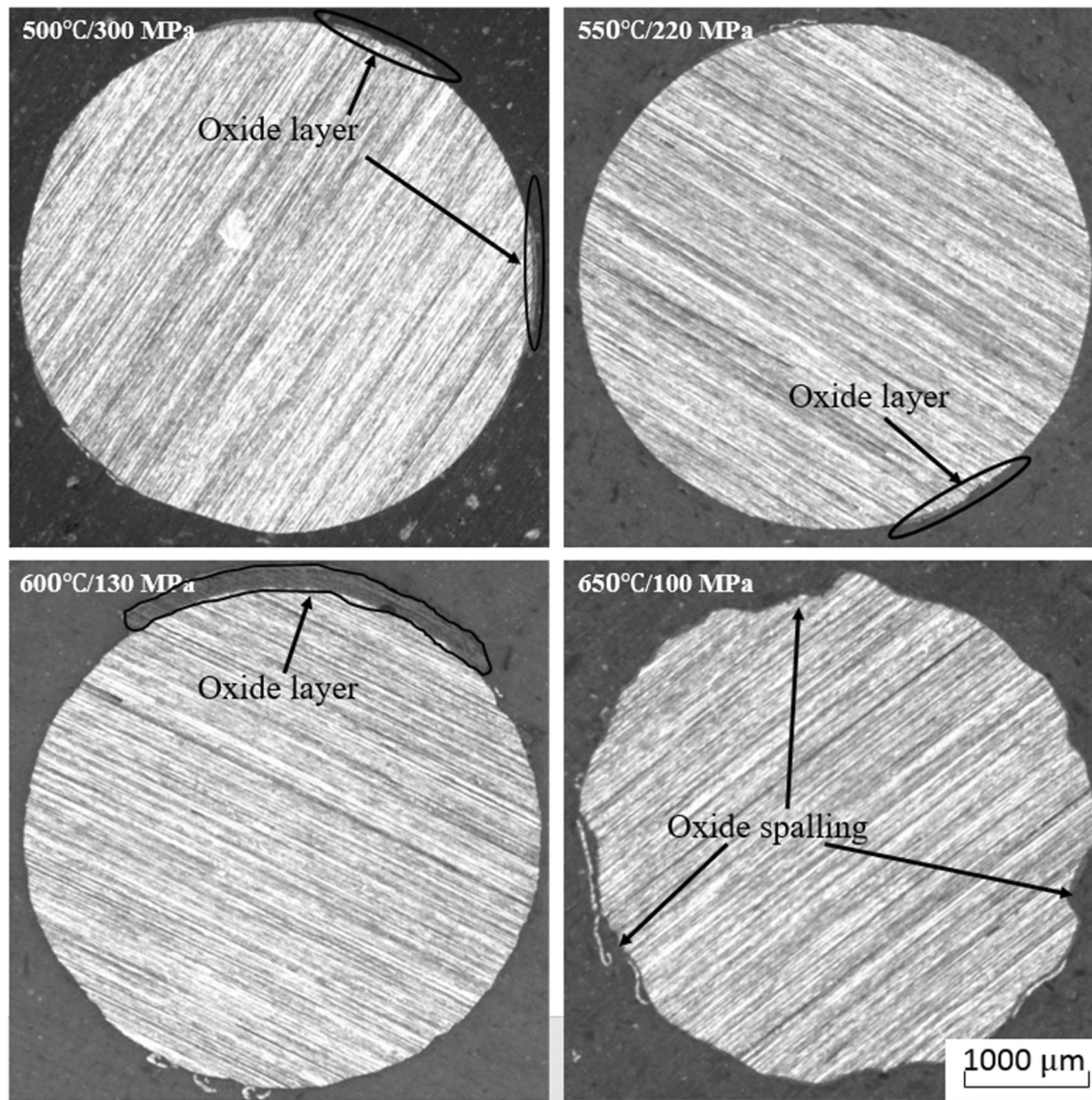
(a)
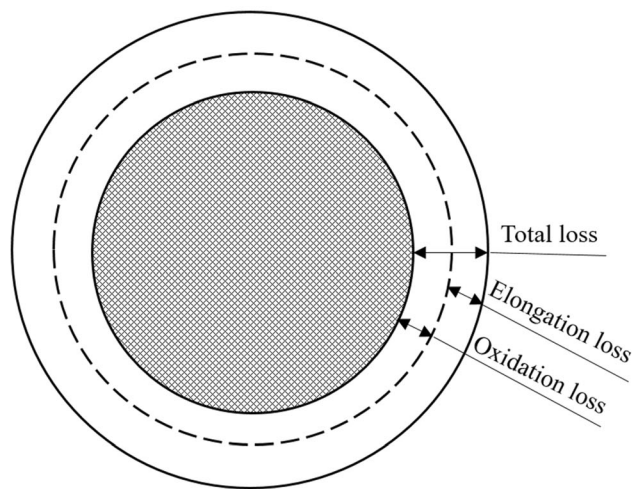
(b)

Fig. 1—(*a*) Cross sections of ruptured F91 coupons observed under an optical microscope showing oxide scale formation on the coupon surfaces; (*b*) schematic of creep coupon cross-section area reduction with the shadow area representing the remaining unoxidized cross section.

shows the necking phenomena on two ruptured coupons, 723 K (500 °C)/280 MPa, and 873 K (600 °C)/130 MPa. The creep curves for these two test conditions are shown in Figure 4. Although with necking the final elongation strains are similar for all the F91 crept coupons, the strain levels at which necking started are different. Necking occurred due to deformation instability by which the specimen elongation would increase suddenly; therefore, a critical strain failure criterion should be defined just before necking, which marks the end of stable creep deformation. It was observed that necking almost occurred for all the specimens at 90 pct of the total time-to-rupture (TTR), and hence the critical failure strain, ε_{cr}, is defined to be at 90 pct TTR. This is an engineering definition for the purpose of creep life prediction. Rigorously, necking should be defined at a time when the local area reduction becomes non-proportional to the axial elongation, but this requires simultaneous measurement of the change in cross-section area, which is rarely done
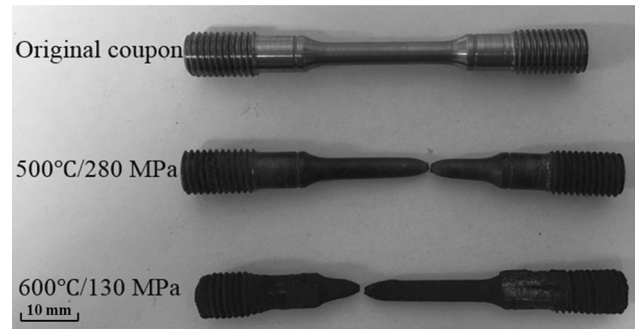

Fig. 3—Ruptured F91 coupons show pronounced necking behavior.

Table II. Summary of Oxidation Loss and Oxide Rate Coefficient K_{ox}

| Temp (°C)	Stress (MPa)	TTR (h)	Nominal Diameter at Rupture (μm)	Total Loss (μm)	Elongation Loss (μm)	Oxidation Loss (μm)	K_{ox} per Test (μm^2/h)	Average K_{ox} per Temperature (μm^2/h)
500	280	4223.9	3925.61	17.19	14.88	2.31	6.34E−04	9.37E−03
	300	3503.7	3917.68	21.16	14.85	6.31	5.69E−03	
	320	2142.5	3911.03	24.48	14.82	9.67	2.18E−02	
550	220	891.4	3895.10	32.45	23.22	9.24	4.78E−02	1.96E−01
	240	306	3893.18	33.41	24.62	8.79	1.26E−01	
	260	81.3	3894.72	32.64	24.45	8.19	4.13E−01	
600	130	1602	3752.34	103.83	63.17	40.66	5.16E−01	4.25E−01
	140	833.6	3773.93	93.03	63.40	29.63	5.27E−01	
	160	180.6	3814.96	72.52	63.34	9.18	2.33E−01	
650	80	873.4	3792.31	83.85	68.12	15.72	1.41E−01	6.56E−01
	100	244.8	3793.66	83.17	68.04	15.13	4.68E−01	
	110	78.8	3794.09	82.95	68.32	14.63	1.36E + 00	

$$y = -19698x + 21.436$$
$$R^2 = 0.8657$$
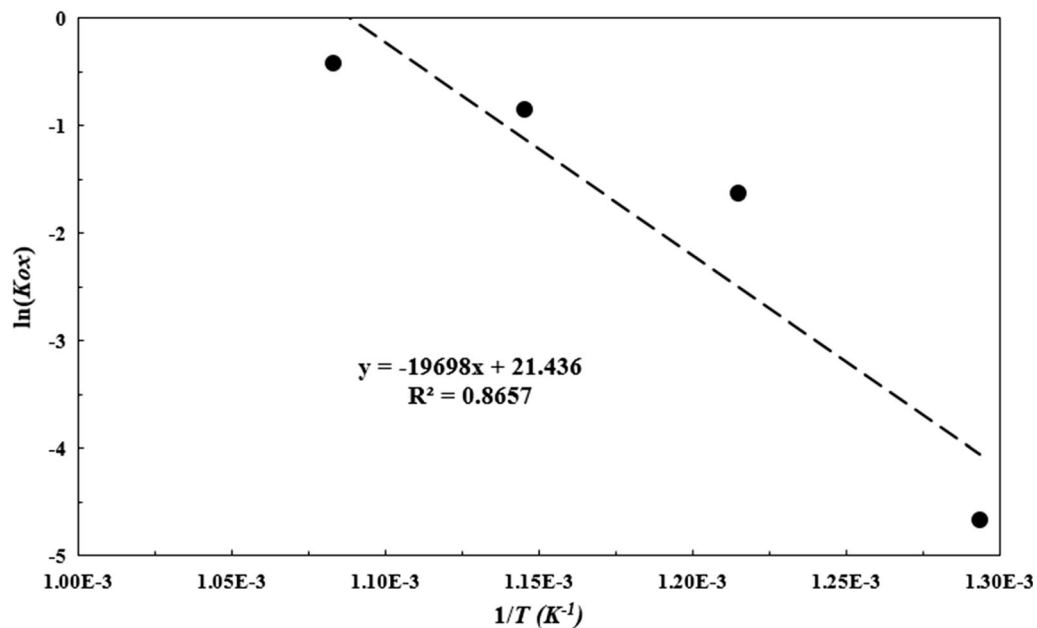
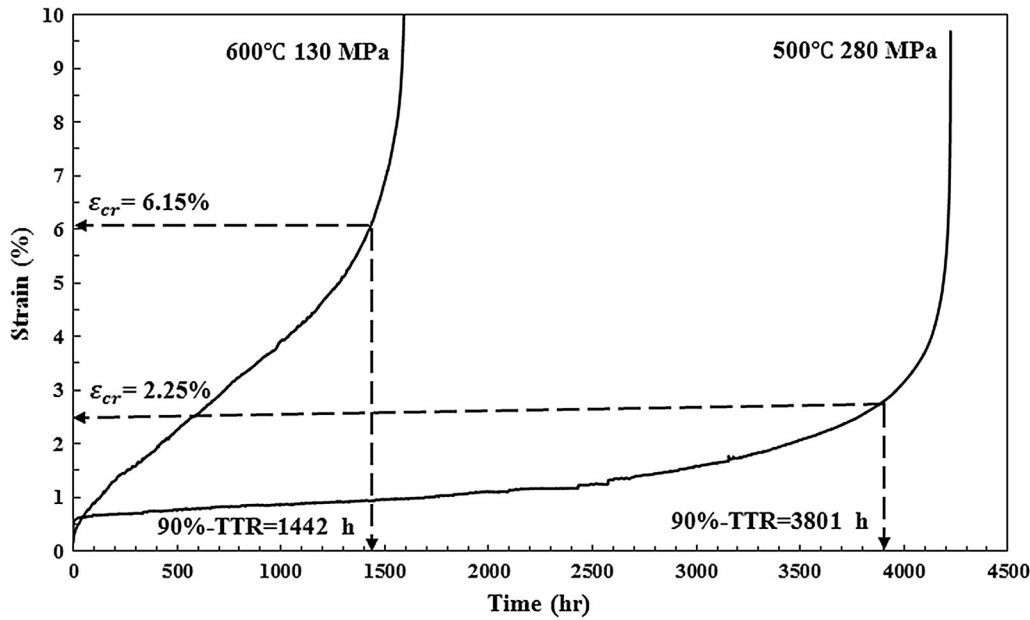Fig. 2—K_{ox} Arrhenius plot for activation energy and proportional constant determination.

Fig. 4—90 pct TTR associated with strain.

Table III. Minimum Creep Rates, Critical Strains, and 90 Pct TTR for F91 Steel

Temp (°C)	Stress (MPa)	$\dot{\varepsilon}_{ss}$ (h^{-1})	TTR (h)	90 pct TTR (h)	Strain at 90 Pct TTR	Average ε_{cr}
500	280	2.31E−6	4223.8	3801.42	0.022	0.02
	300	2.38E−6	3503.7	3153.33	0.02	
	320	4.99E−06	2142.5	1928.25	0.02	
550	220	4.61E−5	891.4	802.26	0.054	0.06
	240	1.09E−4	305.0	274.5	0.055	
	260	4.99E−04	81.3	73.17	0.072	
600	130	3.00E−5	1602.0	1441.8	0.084	0.066
	140	6.24E−5	833.6	750.24	0.054	
	160	3.42E−04	180.6	162.54	0.062	
650	80	4.45E−5	873.4	786.06	0.063	0.068
	100	1.82E−4	244.8	220.32	0.064	
	110	7.98E−04	78.8	70.92	0.078	

during creep testing. It is unpractical using lateral strain gauge to capture necking due to the fact that the necking location is often unpredictable when deformation instability occurs. Nonetheless, 90 pct TTR for necking should be acceptable for engineering purposes, particularly because microstructural non-uniformity in a real material often exceeds 10 pct. Table II summarizes ε_{cr} at 90 pct TTR of F91 ruptured coupons at various temperatures. It is noted that there is an increase in critical strain, ε_{cr}, from ~ 2 to ~ 6-7 pct above 723 K (500 °C). This phenomenon indicates that there is a "brittle-to-ductile" transition in creep necking. In the present study, the same trend of ε_{cr} for F91 is assumed to be true for all Grade 91 steels, owing to their similar composition and microstructure. The minimum creep rate ($\dot{\varepsilon}_{ss}$), TTR, and critical failure strains of the F91 under various test conditions are summarized in Table III. These data will be used for model validation.

C. Creep Curves

With the inclusion of the oxidation effect as expressed by Eqs. [7a] through [10a], the modified DMTS equation is used to depict F91 creep behavior, as illustrated in Figures 5 through 8 with TTR over 300 hours. Table IV lists the model parameters in Eqs. [10a] through [10c]. Note that the dislocation multiplication factor (M) was obtained by fitting the basic DMTS model to the MCrAlY-coated F91 creep behavior (without the influence of oxidation).[26]

In general, the modified DMTS model improves the creep predictions of F91 at all temperatures from 773 K to 923 K (500 °C to 650 °C). First of all, the minimum creep rate $\dot{\varepsilon}_{ss}$ is increased because of the oxidation effect, indicating that oxidation is an external contributing factor, in addition to the material-intrinsic deformation mechanisms, GBS, IDC, and IDG. The matching with the experimental observation validates the modified
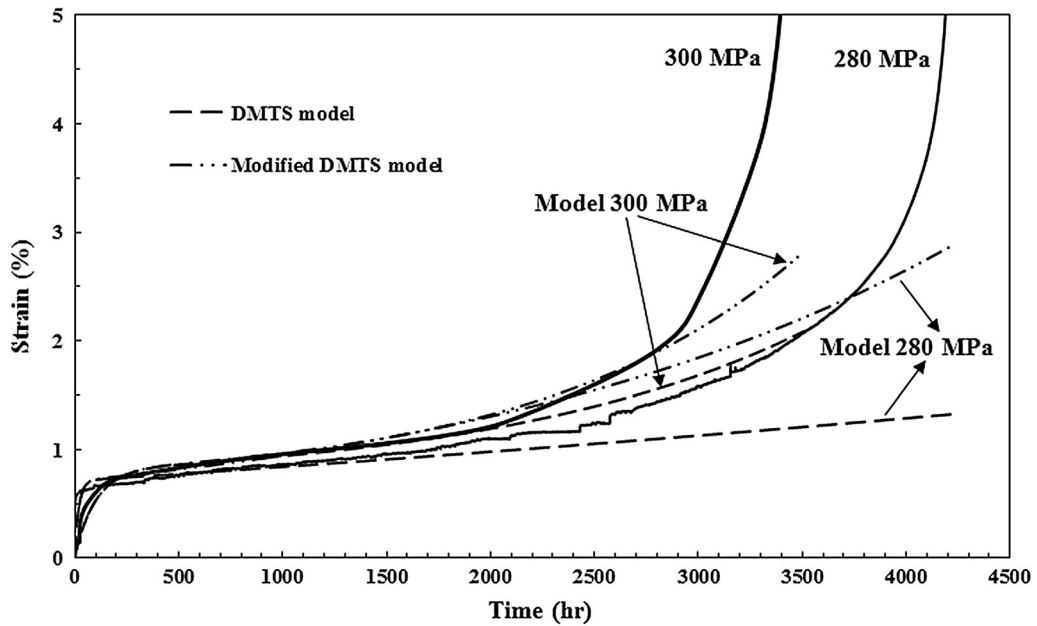
Fig. 5—Comparison between basic and modified DMTS models for creep strain–time curves of F91 coupons at 500 °C.
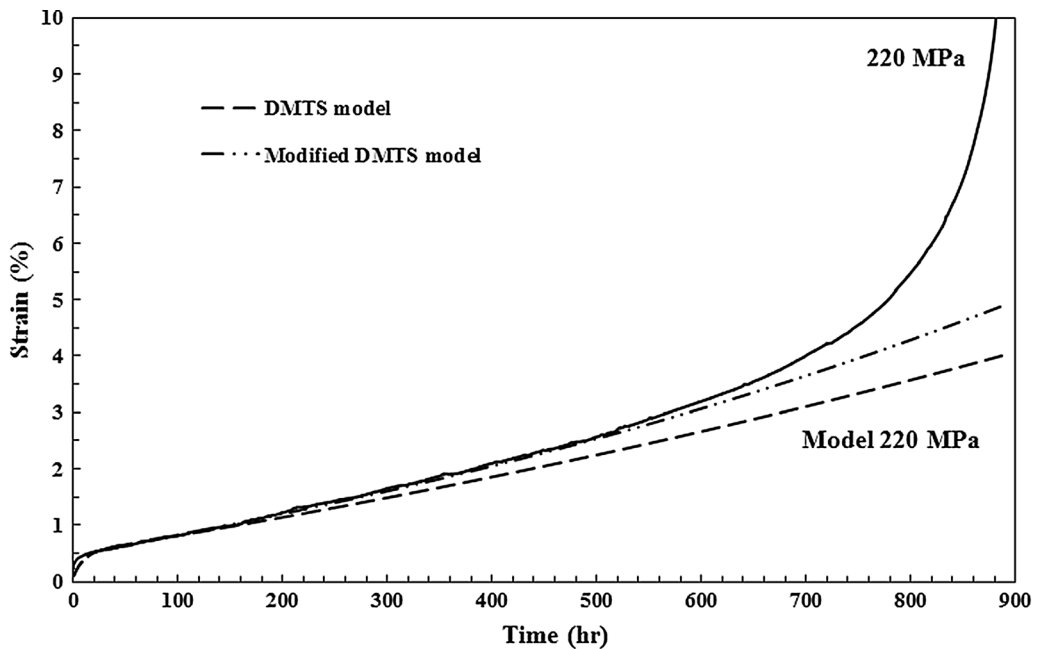

Fig. 6—Comparison between basic and modified DMTS models for creep strain–time curves of F91 coupons at 550 °C.

DMTS model. In particular, for longer time creep, where the oxide growth becomes increasingly influential, the modified DMTS describes the creep behavior better than the basic DMTS model, although the two models have little difference for short-term creep tests. At 650 °C, oxidation is the most severe, Eq. [9] tends to exacerbate the oxidation effect by the conservative simplification. However, because failure strain is defined prior to instability, the creep life prediction still matches closely to experimental observation. This implies that oxidation can contribute significantly to the deviation toward long-term creep, which has not been emphasized much in other creep life prediction models reported in the literature.
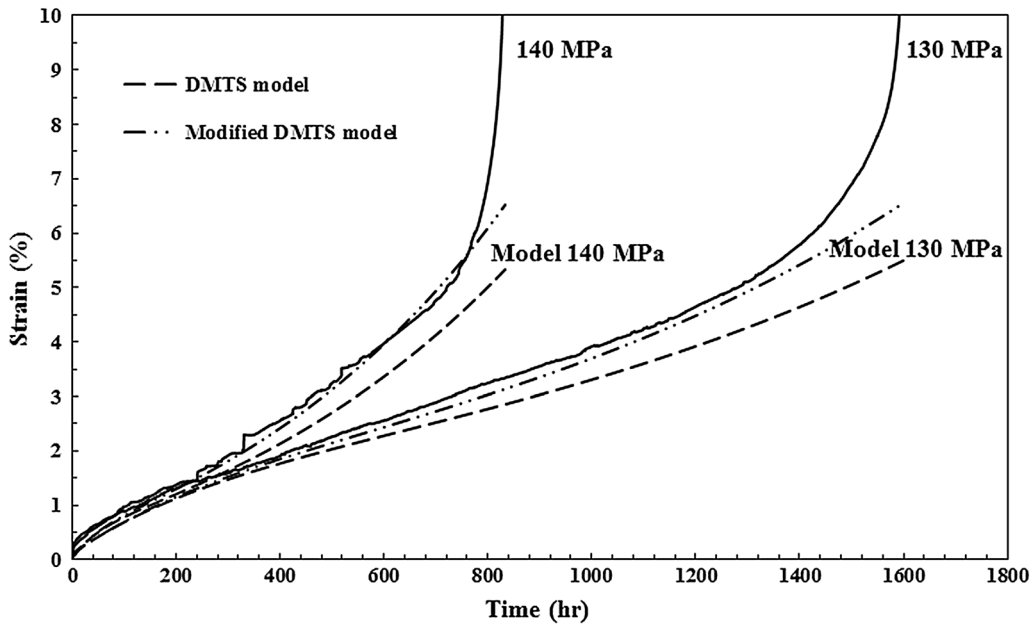
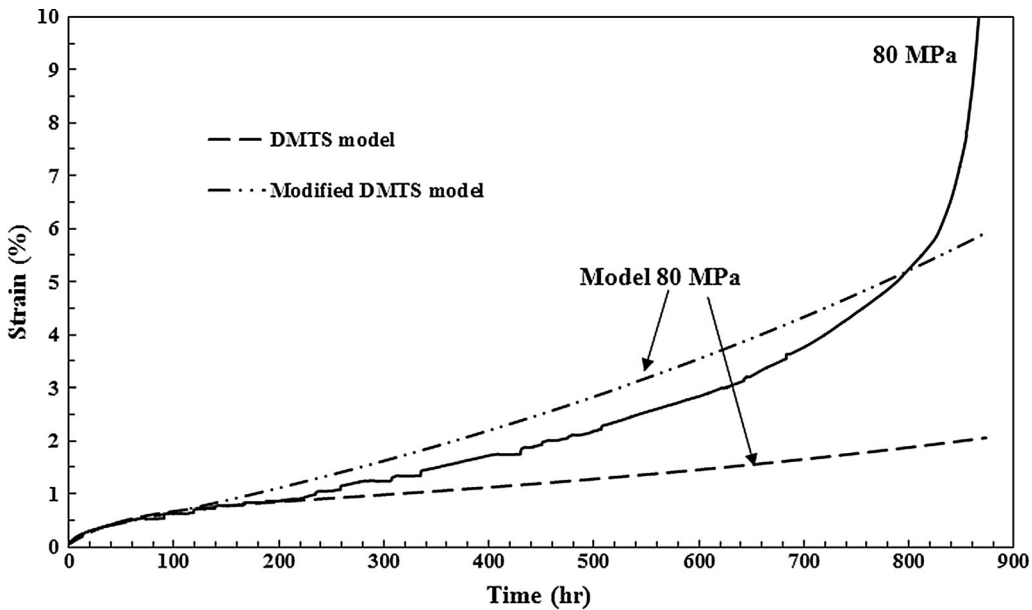Fig. 7—Comparison between basic and modified DMTS models for creep strain–time curves of F91 coupons at 600 °C.

Fig. 8—Comparison between basic and modified DMTS models for creep strain–time curves of F91 coupons at 650 °C.

D. Long-Term Creep Life Prediction

With the inclusion of the oxidation effect, the modified DMTS model improves the accuracy of long-term creep life prediction using Eq. [11], as illustrated in Figures 9 through 12 for NIMS Grade 91 steels, in comparison with the basic DMTS model; the R^2 values indicated the accuracy of each model prediction. For MgB (plate) which is the closest to F91 in terms of composition and heat treatment, the modified DMTS model shows marked improvement in the coefficient of determination from 0.89 to 0.99. For the other Grade 91 steels, the R^2 values of the two models appear to be equally good (above 0.95). Since most of the available creep rupture data were obtained at TTR $< 10^4$ hours, it is critical to ensure that the long-term extrapolation has considered the participating deformation and damage mechanisms. The creep life plots show that the two models have similar performance for TTR$< 10^4$ hours. The difference starts to show up at creep times over ~ 10^4 hours. Actually, the modified DMTS model describes the "life breakdown" phenomenon in agreement with the experimental observations for long-term creep. The discrepancy of the basic DMTS model arises for long-term creep because of missing consideration of

Table IV. Strain–Time Curve Model Parameters

Temp (°C)	Stress (MPa)	Work-Hardening Coefficient H (GPa)	Dislocation Multiplication Factor (M)	Transient Shape Parameter (β)
500	320	47.16	1000	1.008
	300			
	280			
550	260	41.15	200	
	240			
	220			
600	160	25.41	110	
	140			
	130			
650	110	8.58	5	
	100			
	80			

Fig. 9—Comparison between basic and modified DMTS models for life prediction of MgB, a designation by NIMS for a Grade 91 plate material (symbols: experimental; solid lines: DMTS model; dash lines: modified DMTS model).

the oxidation effect. On the mechanism basis, the phenomena are the results of creep-oxidation interaction, rather than the artificially divided "two stress regions."[21] No empirical model can truly predict the long-term creep performance with oxidation influence.

For creep life prediction, the Larson–Miller parameter (LMP) method is one of the most popular methods in industrial applications. In this method, the creep rupture data are presented in a plot as function of the applied (norminal) stress against a temperature-compensated parameter, called the Larson–Miller parameter P_{LM} (1952) [6]:

$$P_{LM} = T(\log t_r + C_{LM}), \qquad [14]$$

where T is absolute temperature; t_r is time-to-rupture (TTR), and C_{LM} is the LMP constant. The relationships are often established through polynomial fitting.

In order to establish the correlations between the applied stress and TTR, a large amount of data are needed to construct the LMP plot.[6,21,27] For the purpose of quick assessment of creep strength, high stresses are often used to obtain short-term TTR data, but extrapolation using a polynomial equation is not reliable beyond the fitted data range. This is why creep life prediction by the LMP method still needs long-term creep test data which are time-consuming and costly to obtain. In addition, from the deformation-mechanism point of view, creep tests conducted at either higher stress or higher temperature may induce different dominant deformation mechanism(s) from the one(s) under the service loading condition. Therefore, empirical methods of creep life prediction by extrapolation from short-term creep test data without deformation-mechanism specification are not reliable. The
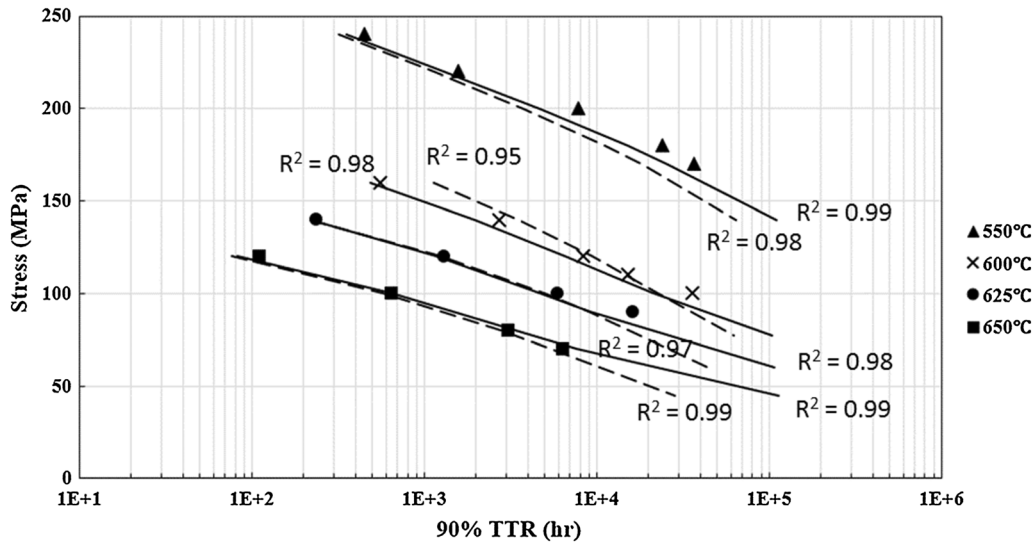
Fig. 10—Comparison between basic and modified DMTS models for life prediction of MgD, a designation by NIMS for another Grade 91 plate material (symbols: experimental; solid lines: DMTS model; dash lines: modified DMTS model).
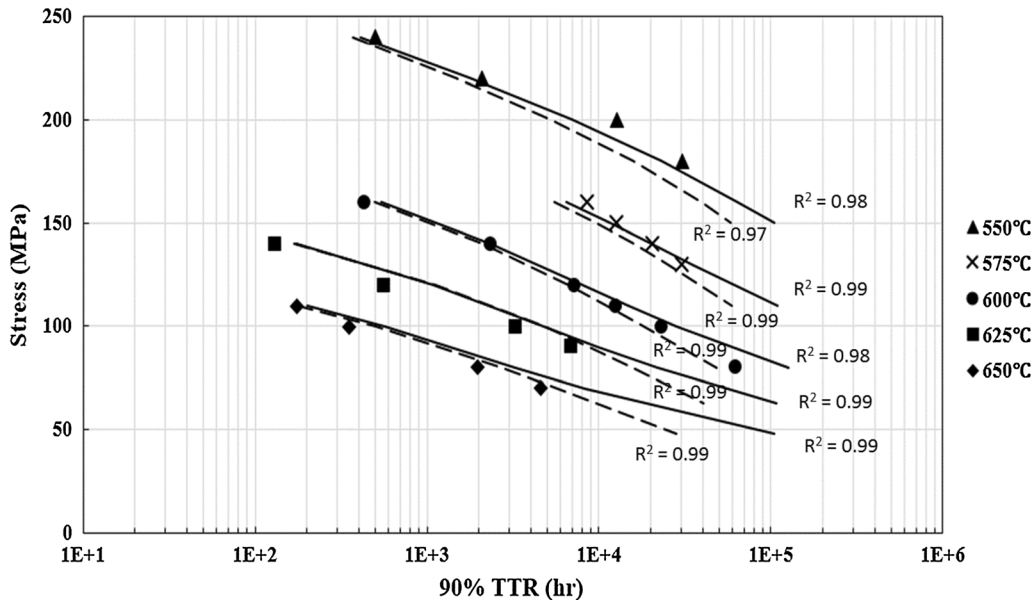

Fig. 11—Comparison between basic and modified DMTS models for life prediction of MGD, a designation by NIMS for a Grade 91 tube material (symbols: experimental; solid lines: DMTS model; dash lines: modified DMTS model).

modified DMTS model is, on the other hand, validated with consideration of participating deformation and damage mechanisms, which ensures the validity and accuracy of creep life prediction from short-term to long-term creep.

The predicted creep lives of NIMS Plate MgB by the modified DMTS model are depicted in an LMP plot in order to compare with the experimental 90 pct-TTR data. The Larson–Miller constant, C_{LM}, in Eq. [14] is 33.[27] As shown in Figure 13, the predicted lives all agree with the experimental data very well. Moreover, each creep rupture failure mode can be identified by the modified DMTS model, in a manner showing the partitioning portions of the three mechanisms: GBS,

IDG, and IDC. Figure 14 shows two microstructures at creep rupture: one crept under 873 K (600 °C)/160 MPa, and the other crept under 923 K (650 °C)/100 MPa, with the associated mechanism pie-charts, which are made up by the ratio of the minimum creep rate per mechanism to the total strain rate under the given test condition. In the 873 K (600 °C)/160 MPa case, GBS predominated (~ 94 pct) and the microstructure retained its original lath structure, whereas in the 923 K (650 °C)/100 MPa case, the model predicts that a significant portion (~ 38 pct) of creep deformation occurred by IDC. Accordingly, the lath structure did become more elongated. It should be noted that the mechanism pie-chart is made based on the minimum creep rate which occurred at the fairly
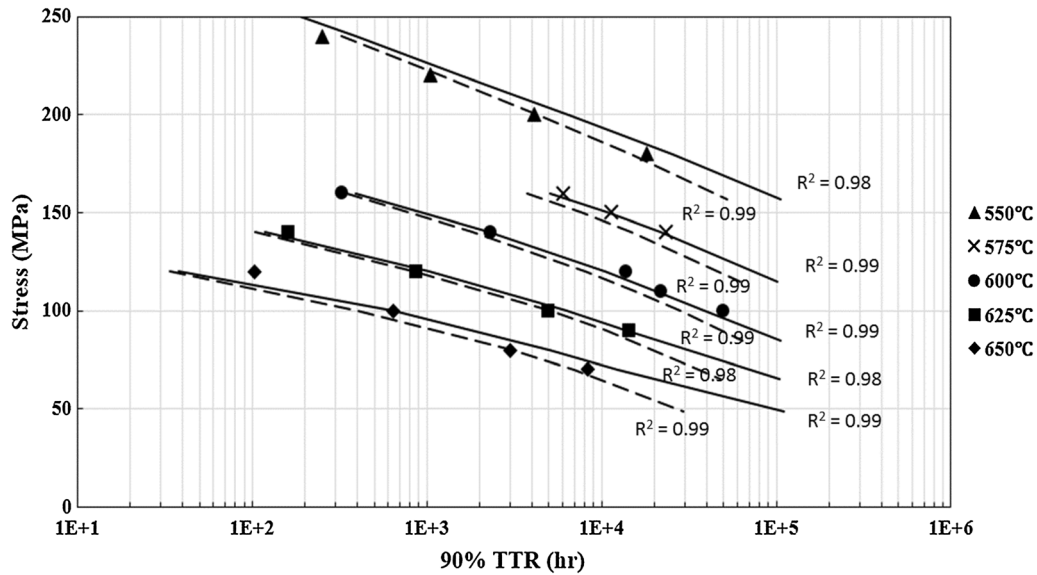
Fig. 12—Comparison between basic and modified DMTS models for life prediction of MGQ, a designation by NIMS for a Grade 91 pipe material (symbols: experimental; solid lines: DMTS model; dash lines: modified DMTS model).
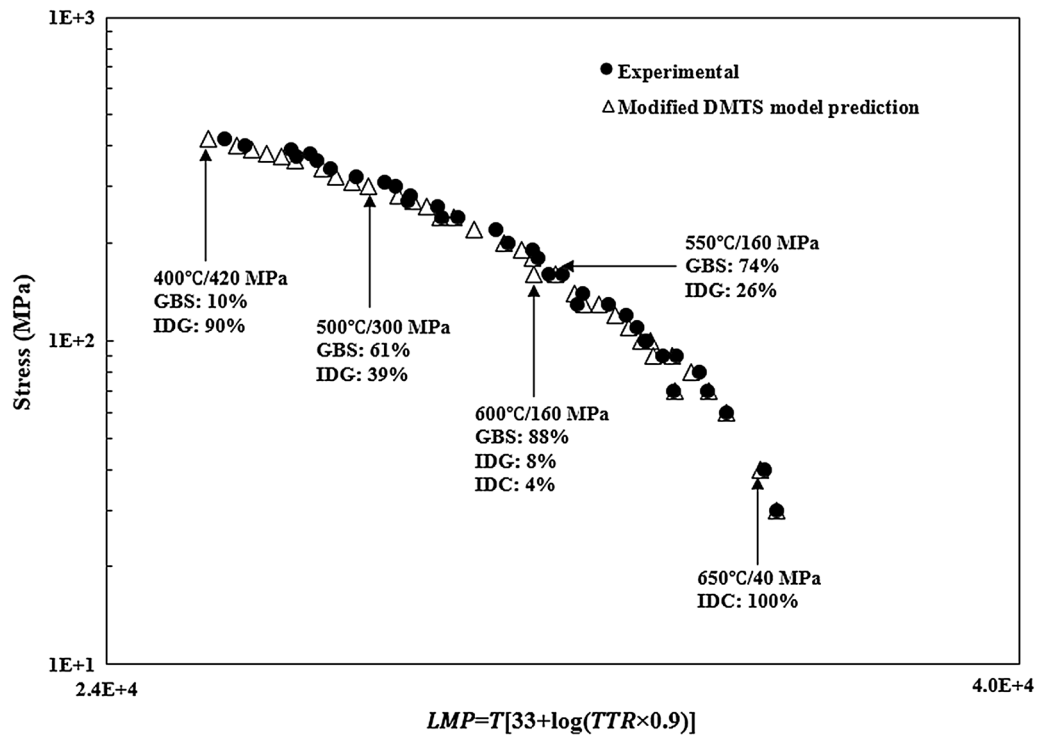

Fig. 13—The modified DMTS model prediction of NIMS Plate MgB in LMP plot with experimental data for comparison.

early stage. As the creep process continued to the end, the instantaneous creep rate would increase significantly due to intervention of tertiary creep mechanisms. Therefore, in the 923 K (650 °C)/100 MPa case, IDC became even more dominant toward the end. The metallurgical evidence supports the model prediction. Using the modified DMTS model, such pie-charts can be obtained for every creep condition. More detailed studies, perhaps through artificial intelligence (AI)-assisted microstructural feature recognition, are needed to correlate the ratio of mechanism partitioning with the deformed microstructural features for further work. It is significant that the modified DMTS model can provide engineers a useful means to better understand the physics of creep failure and identify the failure modes in quantitative details, and furthermore to tailor the material and component design for better performance, whereas the LMP plot does not provide such
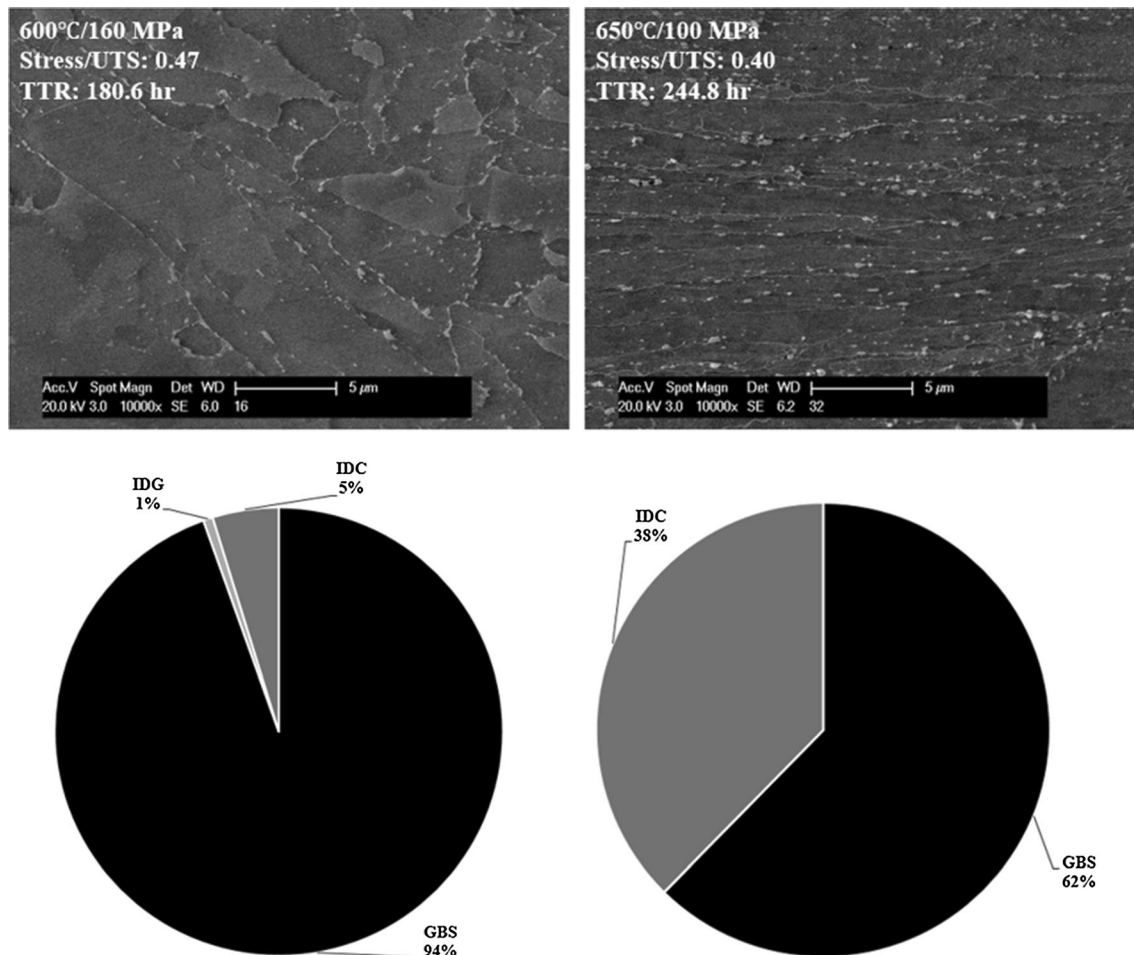
Fig. 14—Microstructural analyses with mechanism indication pie-charts.

detailed information, from a life prediction point of view.

IV. CONCLUSIONS

In this study, the modified DMTS model is developed based on the well-recognized deformation mechanisms coupled with the parabolic oxidation law. The model is validated with F91 creep data from 773 K to 923 K (500 °C to 650 °C) at various stress levels. Also, a long-term creep life prediction equation is derived from the mechanism-based formulation. In particular, the following conclusions can be drawn:

- For the first time, the present study proposed an area-deduction method to quantify oxide scale growth during creep. From such measurements, the oxidation growth rate coefficient, K_{ox}, is determined. In the present study, the average K_{ox} at a temperature is assumed to obey the Arrhenius relationship, but the method can be used for further quantification of the influence of stress.
- From short-term creep curve analyses, the critical failure strain ε_{cr} was established at 90 pct TTR, just prior to the onset of unstable deformation when

necking occurred to cause the final rupture. This critical failure strain exhibited a temperature-dependent "brittle-to-ductile" transition: ε_{cr} = 2-3 pct over the temperature range of 723-773 K (450-500 °C); and ε_{cr} = 6-7 pct over the temperature above 773 K (500 °C). This failure criterion was used for long-term creep life prediction of modified Grade 91 steels.

- By taking oxidation effect into account, the modified DMTS model better describes the creep curve of F91 coupons than the basic DMTS model with coupon-borne oxidation influence. In addition, the modified DMTS model also predicts the long-term creep lives of Grade 91 steels in excellent agreement with NIMS creep data. This signifies the importance of the separation of oxidation effect from material-intrinsic deformation mechanisms such as IDG, IDC, and GBS.
- The modified DMTS model is also compared with the Larson–Miller parameter method. Since this model is developed on the mechanism basis, it only needs short-term creep data ($< 10^4$ hours) to validate the mechanism contribution. The predictions of the modified DMTS model are shown to be accurate (with coefficient of determination > 95 pct) for the long-term ($>10^4$ hours) creep performance of

modified Grade 91 steels. This saves the effort for long-term creep tests which are very costly and delay the design optimization. In addition, the modified DMTS model also provides insights into the controlling deformation mechanisms and potential failure mode, feeding back information for further material improvement.

REFERENCES

1. E.N. DaC Andrade: *Proc. R. Soc. A*, 1910, vol. 90, pp. 329–42.
2. H.J. Frost and M.F. Ashby: *Deformation-Mechanism Maps*, Pergamon Press, Elmsford, 1982, pp. 1–19.
3. T.G. Langdon: *Philos. Mag. Phil. Mag.*, 1970, vol. 22, pp. 689–700.
4. H. Lüthy, R.A. White, and O.D. Sherby: *Mater. Sci. Eng.*, 1979, vol. 39, pp. 211–16.
5. X.J. Wu and A.K. Koul: *Metall. Mater. Trans. A*, 1995, vol. 26A, pp. 905–14.
6. F. Larson and J. Miller: *Trans. ASME*, 1952, vol. 74, p. 765.
7. F.C. Monkman and N.J. Grant: *ASTM Proc.*, 1956, vol. 56, pp. 593–620.
8. B. Wilshire and P.J. Scharning: *Mater. Sci. Technol.*, 2009, vol. 25, pp. 243–48.
9. Allen and S. Garwood: *Energy Materials-Strategic Research Agenda*. Q2, Materials Energy Review, the Institute of Materials, Minerals and Mining, London, 2007.
10. K. Kimura and Y. Takahashi: Proc. ASME 2012 Press. Vessel. Pip. Conf., 2012, pp. 1–8.
11. K. Kimura, M. Tabuchi, Y. Takahashi, K. Yoshida, and K. Yagi: *Int. J. Microstruct. Mater. Prop.*, 2011, vol. 6, p. 72.
12. K. Kimura and M. Yaguchi: in *Proc. ASME. Pressure Vessels and Piping Conference, Volume 6B: Materials and Fabrication*, 2016, p. 9.
13. J. D. Parker: in *Proc. Sustainable Industrial Processing Summit & Exhibition 2018, Vol. 6, 4–7 November 2018*, Rio De Janeiro, Brazil.
14. M.F. Ashby and B.F. Dyson: *Fracture*, 1984, vol. 84, pp. 3–30.
15. B.F. Dyson and S. Osgerby: *Mater. Sci. Technol.*, 1987, vol. 3, pp. 545–53.
16. X.Z. Zhang, X.J. Wu, R. Liu, J. Liu, and M.X. Yao: *Mater. Sci. Eng. A*, 2017, vol. 689, pp. 345–52.
17. X.J. Wu, S. Williams, and D. Gong: *J. Mater. Eng. Perform.*, 2012, vol. 21, pp. 2255–62.
18. National Institute for Materials Science (Japan): Creep Data Sheet (CDS), No. 43A, 10 Oct 2016.
19. M. Danielewski: *Solid State Phenom.*, 1992, vol. 21&22, pp. 103–34.
20. B.F. Dyson and T.B. Gibbons: *Acta Metall.*, 1987, vol. 35, pp. 2355–69.
21. F. Abe: *Metall. Mater. Trans. A*, 2015, vol. 46A, pp. 5610–25.
22. F. Abe: *Mater. Sci. Eng. A*, 2004, vols. 387–389, pp. 565–69.
23. F. Abe, M. Taneike, and K. Sawada: *Int. J. Press. Vessel. Pip.*, 2007, vol. 84, pp. 3–12.
24. M. Yurechko, C. Schroer, O. Wedemeyer, A. Skrypnik, and J. Konys: *J. Nucl. Mater.*, 2011, vol. 419, pp. 320–28.
25. P. Mathiazhagan and S. Khanna: *High Temp. Mater. Proc.*, 2011, vols. 1–2, pp. 43–50.
26. X.Z. Zhang, X.J. Wu, R. Liu, and M.X. Yao: *Mater. Sci. Eng. A*, 2019, vol. 743, pp. 418–24.
27. T. Shrestha, M. Basirat, I. Charit, G.P. Potirniche, and K.K. Rink: *Mater. Sci. Eng. A*, 2013, vol. 565, pp. 382–91.

Publisher's Note Springer Nature remains neutral with regard to jurisdictional claims in published maps and institutional affiliations.